Chinese Journal of Aeronautics, (2026), **39**(10): 104231

Chinese Society of Aeronautics and Astronautics
& Beihang University

Chinese Journal of Aeronautics

cja@buaa.edu.cn
www.sciencedirect.com

FULL LENGTH ARTICLE

Impact of tip rounding on riblet drag-reduction performance

Stefano CIPELLI [a,*], Giacomo RONCHETTI [b], Davide GATTI [a]

[a] *Institute of Fluid Mechanics, Karlsruhe Institute of Technology, Kaiserstraße 10, Karlsruhe, Baden-Württemberg, Germany*
[b] *Dept. of Aerospace Engineering, Politecnico di Milano, Campus Bovisa, via La Masa 34, Milano 20156, Italy*

Received 5 January 2026; revised 27 January 2026; accepted 16 March 2026
Available online 19 May 2026

KEYWORDS

Riblets;
Drag reduction;
Turbulence;
Direct numerical simulation;
Immersed boundary

Abstract The present paper investigates the effect of tip rounding on the performance of riblets in turbulent flows. The rounding impact is investigated both with Stokes and turbulent simulations, to evaluate the protrusion heights difference Δh and the roughness function ΔU^+, respectively. Three different cross section shapes are considered through inexpensive Stokes simulations, triangular riblets with a $30^\circ, 60^\circ$ and 90° tip angle, and an exponential decay in the Δh value for increasingly larger tip roundings is observed. For the turbulent problem we employ an innovative, cost-effective immersed-boundary method that uses the pre-computed Stokes solution to assemble the immersed-boundary coefficients, enabling an accurate representation of the near-tip flow on relatively coarse grids. Turbulent direct numerical simulations carried out for the 60° geometry reproduce the same trend observed in Stokes calculations, showing that the loss of turbulent drag-reduction due to tip rounding is explained by the geometry's diminished viscous efficiency.

1. Introduction

Riblets are small, streamwise-aligned grooves that reduce skin-friction drag compared with a smooth surface,[1,2] and have been adopted in some aerospace applications to improve fuel efficiency. Typical straight cross sections are triangular, blade, or parabolic. Their effectiveness depends on their size relative to a characteristic turbulent length scale close to the wall, the so-called viscous units, which are defined based on the velocity scale $u_\tau = (\tau_w/\rho)^{1/2}$ and the length scale $\delta_\nu = \nu/u_\tau$. Here, τ_w is the wall shear stress, ν is the kinematic viscosity and ρ the fluid density. The non-dimensional riblet size is l_g^+ (the square root of the groove area in viscous units). Empirically, riblets generate net drag reduction for $l_g^+ \lesssim 18$, whereas larger riblets tend to increase drag.

The effect of riblets is effectively to oppose different resistance to streamwise flow, typically associated with the mean velocity, and to spanwise and wall-normal motions, typically

* Corresponding author.
E-mail address: stefano.cipelli@kit.edu (S. CIPELLI).

☆ This article is part of a special issue entitled: 'Next-Gen Aerospace Complex Surfaces' published in Chinese Journal of Aeronautics. Peer review under responsibility of Editorial Committee of CJA.

ELSEVIER Production and hosting by Elsevier

https://doi.org/10.1016/j.cja.2026.104231
1000-9361

associated with turbulent fluctuations. This effect can be modeled with the introduction of virtual origin for the mean and turbulent flows.[3] The mean flow perceives an equivalent smooth wall at a distance of l_U^+ below the tip, while turbulence senses a closer origin $l_T^+ < l_U^+$. These protrusion heights are directly linked to their roughness function ΔU^+, a measure of drag change consisting in the vertical shift in the mean velocity profile in its logarithmic region induced by a rough surface. For riblets $\Delta U^+ = l_T^+ - l_U^+$, showing that riblets are able to yield negative values of ΔU^+, i.e. yield drag reduction.

The viscous mechanism originally proposed by Luchini et al.[4] and verified experimentally by Bechert et al.[5] dominates when riblets are embedded in the viscous sublayer and can be captured by steady Stokes flows computed in the longitudinal and transverse directions. The distances from the tip to the virtual origins, l_X and l_Y, and their difference Δl quantify a geometry's viscous effectiveness; for very small riblets $\Delta U^+ = -\Delta l^+$, or, in dimensionless form using $h_X = l_X/l_g$, $h_Y = l_Y/l_g, \Delta U^+ = -\Delta h\, l_g^+$, valid roughly for $l_g^+ < 8$.

As riblet size increases, viscous drag reduction is counteracted by drag-increasing mechanisms (increased momentum mixing, secondary motions[6,7] and Kelvin–Helmholtz–like rollers[8,9]), leading to vanishing benefit near $l_g^+ \sim 18$ and to fully-rough behaviour for larger l_g^+;[10] at even larger sizes the roughness function becomes independent of the viscous size.[11]

In practice, manufacturing and wear produce non-ideal features (rounded tips, surface defects) that can degrade performance and reduce the expected fuel savings. To date, and to the authors' knowledge, only García-Mayoral and Jiménez[12] has addressed tip rounding: in the Stokes limit they compared protrusion heights for triangular and blade riblets with corner radii up to 15% of the spacing, finding that Δh decreases with rounding for triangular shapes (while blade cases showed slight increases). Because Δh correlates with ΔU^+, rounding is expected to reduce drag-reduction potential, but a direct turbulent assessment is missing.

This paper quantifies performance degradation from tip rounding in both the Stokes limit and in turbulent channel flows. The Stokes study examines triangular cross sections with different tip angles to assess geometric sensitivity; the turbulent study focuses on a single cross section at two viscous sizes while varying the tip radius, with the aim of comparing viscous predictions to DNS results. Section 2 presents the numerical approach (a discrete-forcing IBM plus a Stokes-informed corner-correction for turbulent cases). Section 3 reports longitudinal and transverse protrusion heights and viscous performance loss, and Section 4 compares DNS results for the selected geometry with the Stokes-based predictions.

2. Method

The DNS code used for all simulations was introduced by Luchini,[13] and solves the incompressible Navier–Stokes equations written in primitive variables on a staggered Cartesian grid in a channel geometry. Second-order finite differences are used in every direction. The momentum equation is advanced in time by a fractional time stepping method using a third-order Runge–Kutta (RK3) scheme,[14] adapting the timestep to maintain a constant CFL number. The time advancement is explicit, except for the treatment of the immersed boundary forcing terms. The Poisson equation for pressure is solved by an iterative Successive Over-Relaxation (known as SOR) algorithm applied to a Gauss–Seidel red–black iteration. The walls are dealt with via an immersed-boundary method, and, for the turbulent cases, a Corner-Correction (COCO) is used to modify the immersed boundary forcing to enhance the accuracy in proximity of the riblet tips. Such algorithms based on low-order finite-differences and the use of an IBM are now standard in the context of direct numerical simulations of turbulent channel flows.[6,15] The use of the corner-correction enables the correct resolution of flows around small and possibly sharp geometric features with a moderate number of points, while resolving the flow in such cases would require an almost infinite grid resolution.[16] This method hinges on the fact that, close to solid boundaries, and particularly close to geometric singularities, unsteady and non-linear effects are higher order with respect to viscous ones. For this reason, the local velocity field in a turbulent flow will resemble the steady Stokes solution around the same geometry. While a canonical IBM can at best, in the context of second-order accurate schemes, enforce a velocity field which depends linearly on the wall distance, the corner-correction can enforce the steady Stokes solution, significantly increasing the accuracy of the solver. In this section we will show how the immersed boundary and corner-correction are introduced into the Navier–Stokes equations.

Eq. (1) presents the incompressible Navier–Stokes momentum equation for the jth velocity component (u_j), incorporating a deferred correction term $\mathscr{F}_j$ representing the discrete-forcing IBM. As we will observe, the deferred correction can either introduce a second-order accurate representation of the boundary as in the canonical IBM from Luchini et al.,[17] or can be used to enforce the corner-correction. We will later prove how the deferred correction term can be written as a linear function of u_j, with proportionality constant $\nu\lambda$, being λ the IBM/COCO coefficient.

$$\frac{\partial u_j}{\partial t} = -\frac{\partial}{\partial x_i}\left(u_i u_j\right) - \frac{1}{\rho}\cdot\frac{\partial p}{\partial x_j} + \nu\frac{\partial^2 u_j}{\partial x_i \partial x_i} + \mathscr{F}_j \tag{1}$$

Eq. (1) is discretized in time using a third order Runge–Kutta scheme, as shown for the predictor step (solved for $u_j^{*,n+\frac{k}{3}}$) in Eq. (2) for a timestep n and the kth RK stage. The convective, pressure gradient and viscous terms of Eq. (1) are represented by the f_j term, while the deferred correction term ($\mathscr{F}_j = -\nu\lambda u_j$) is discretized with an implicit Euler scheme for simplicity. Note that also integrating such term exactly is possible to retain the second-order time accuracy of the scheme. For more details refer to Luchini et al.[17]

$$u_j^{*,n+\frac{k}{3}} = \frac{1}{1+\Delta t\,\nu\,\lambda(a_k+b_k)}\left[u_j^{n+\frac{k-1}{3}} + \Delta t\left(a_k f_j^{n+\frac{k-1}{3}} + b_k f_j^{n+\frac{k-2}{3}}\right)\right] \tag{2}$$

The a_k, b_k coefficients are defined according to Rai and Moin.[14]

The procedure used to calculate the deferred correction term is summarized in the following part of the section for the IBM and COCO cases. The corner-correction is applied in the proximity of riblet tips to improve the accuracy, while the canonical immersed boundary is applied for the rest of the points whose stencil intersects the boundary. The underlying idea of the deferred correction is that the Navier–Stokes equations are written for a simple "staircase" approximation of the boundary, meaning that no discretization coefficient is modified to incorporate the actual distance of a point from the boundary, and points external to the fluid region present zero velocity. What yields a more accurate representation of the boundary is a deferred correction term $\mathscr{F}_j$, which is always gauged to the value of the velocity at the present position u_j and has different expressions for the IBM and the COCO cases.

In the immersed boundary from Luchini et al.,[17] the idea is to use the deferred correction to correct the Laplacian term, by assuming that the exact solution we want to impose is a linear function of the wall distance. If we consider for example the Laplacian of a scalar field $\phi(x, y)$, for simplicity, which we aim at correcting with a deferred correction $\mathscr{F}$, we write the 2D Laplace equation for $\phi(x, y) = \phi_{i,j}$ as follows:

$$
\begin{aligned}
&d_x^{(2)}(-1)\phi_{i-1,j} + d_y^{(2)}(-1)\,\phi_{i,j-1} + \left[d_x^{(2)}(0) + d_y^{(2)}(0)\right]\phi_{i,j} \\
&+ d_x^{(2)}(1)\,\phi_{i+1,j} + d_y^{(2)}(1)\,\phi_{i,j+1} = \mathscr{F}
\end{aligned}
\tag{3}
$$

being $d^{(2)}(\cdot)$ the finite difference coefficients for the positive $(+1)$, negative (-1) stencil arms in x and y and for the central stencil point (0), and $\mathscr{F}$ the deferred correction term.

The imposed solution ϕ_e, which vanishes at the boundary, equals $\phi_{i,j}$ at (x_0, y_0) and varies linearly with x and y, is given by

$$
\phi_e(x, y) = \left(1 + \frac{x - x_0}{\delta x} + \frac{y - y_0}{\delta y}\right)\phi_{i,j}
\tag{4}
$$

where δx and δy are the distances from the boundary, as visible from Fig. 1, and the exact solution is function of the discrete solution at position (x, y). If the solution presented in Eq. (4) is input in Eq. (3), the retrieved expression for the deferred correction is the following:

$$
\begin{aligned}
\mathscr{F} = \;& \Big[d_x^{(2)}(0) + d_y^{(2)}(0) + \left(1 + \tfrac{\Delta x}{\delta x}\right) d_x^{(2)}(1) \\
& + \left(1 + \tfrac{\Delta y}{\delta y}\right) d_y^{(2)}(1)\Big]\phi_{i,j}
\end{aligned}
\tag{5}
$$

where $\Delta x, \Delta y$ are the grid spacings and the term in the square brackets is the IBM coefficient $\lambda^{\mathscr{I}}$. When we want to generalize the method to a 3D case, for an arbitrary number of intersections with the boundary, the expression for the IBM coefficient $\lambda^{\mathscr{I}}$ becomes the following:

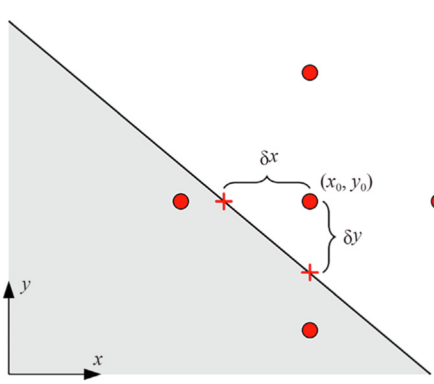

Fig. 1 An example of a computational stencil from a Laplacian centered at coordinates (x_0, y_0), at distances δx and δy from boundary in x and y directions.

$$
\lambda^{\mathscr{I}} = \sum_{l=1}^{3}\left[d_{x_l}^{(2)}(-1)\,\frac{\Delta x_l - \delta x_{l,m}}{\delta x_{l,m}} + d_{x_l}^{(2)}(+1)\,\frac{\Delta x_l - \delta x_{l,p}}{\delta x_{l,p}}\right]
\tag{6}
$$

where $d_{x_l}^{(2)}(\pm 1)$ is the Laplacian discretization coefficient for the x_lth direction (positive: $+1$ or negative: -1), Δx_l is the grid spacing in the x_lth direction ($\Delta x_2 = \Delta y$, for example) and $\delta x_{l,p/m}$ is the distance from the boundary in the positive ($_p$) or negative ($_m$) x_lth direction. When the stencil does not intersect the boundary in the $x_{l,p/m}$th direction, the relationship $\delta x_{l,p/m} = \Delta x_l$ holds. When no stencil arm intersects the boundary, the coefficient is identically zero, and the equation is not modified. On the other hand, when the point gets increasingly closer to the boundary, the coefficient is driven to an infinite value, and, as visible from Eq. (2), the velocity is driven to zero.

The corner-correction can be introduced in a straightforward way by manipulating and combining the momentum equation and the Stokes equation, considering the variables of the Stokes equation as known variables. For a quicker treatment, we will simply define the deferred correction which is enforcing the Stokes solution in proximity of the corners, which is defined as follows for the jth velocity component:

$$
\begin{aligned}
\mathscr{F}_j^{\mathscr{S}} = \nu \Bigg\{ & \sum_{l=1}^{3}\Bigg[d_{x_l}^{(2)}(0) + d_{x_l}^{(2)}(-1)\,\frac{u_j^{\mathscr{S}}(x_l - \Delta x_l)}{u_j^{\mathscr{S}}(x_l)} \\
& + d_{x_l}^{(2)}(+1)\,\frac{u_j^{\mathscr{S}}(x_l + \Delta x_l)}{u_j^{\mathscr{S}}(x_l)}\Bigg] - \frac{1}{\mu}\Bigg[d_{x_j}^{(1)}(1)\,\frac{p^{\mathscr{S}}(x_j + \Delta x_j/2)}{u_j^{\mathscr{S}}(x_j)} \\
& + d_{x_j}^{(1)}(0)\,\frac{p^{\mathscr{S}}(x_j - \Delta x_j/2)}{u_j^{\mathscr{S}}(x_j)}\Bigg]\Bigg\} u_j
\end{aligned}
\tag{7}
$$

In this expression, $u_j^{\mathscr{S}}, p^{\mathscr{S}}$ are the Stokes solution for the jth velocity component and for pressure, x_l represents the position (x, y, z), or the indices (i, j, k), and $x_l \pm \Delta x_l$ represents indices $(i+1, j, k)$ for $l = 1$, for example. The pressure gradient has to be evaluated in the jth direction. The corner-correction coefficient $\lambda_j^{\mathscr{S}}$ is the term inside the curly bracket.

All terms in Eq. (7) are known: the Stokes solution can be computed at low cost, stored, and used to assemble the corner-correction coefficients prior to the turbulent simulation. Note that in Eq. (7) the distance from the boundary in the x_lth direction does not appear explicitly, since it is intrinsically encoded in the pre-computed Stokes solution. An example of this pre-computed field is shown in Fig. 2 for the sharp-tip case with tip angle 60°. The longitudinal ($u^{\mathscr{S}}$) and transverse ($v^{\mathscr{S}}$) components display similar overall patterns; however, $u^{\mathscr{S}}$ penetrates deeper into the grooves—indicative of a larger protrusion height, while $v^{\mathscr{S}}$ attains slightly negative values in the valleys, signalling local flow reversal. Indeed, the combined $v^{\mathscr{S}}$ and $w^{\mathscr{S}}$ (vertical) fields in the cross-plane reveal recirculation regions. Dashed lines in the plots indicate the zero contours of the considered components. The pressure field exhibits a singularity due to the sharp riblet tip that is only partially captured at finite grid resolution.

As apparent from Eq. (7), the evaluation of the COCO coefficient requires the Stokes fields $u_j^{\mathscr{S}}(x_l \pm \Delta x_l)$ and $p^{\mathscr{S}}(x_l \pm \Delta x_l/2)$. For points lying very close to the boundary, the shifted location $(x_l \pm \Delta x_l)$ or $(x_l \pm \Delta x_l/2)$ may fall outside the fluid domain and inside the solid. While it is natural to assume zero velocity outside the fluid, pressure cannot be set to zero without introducing an unphysical discontinuity at

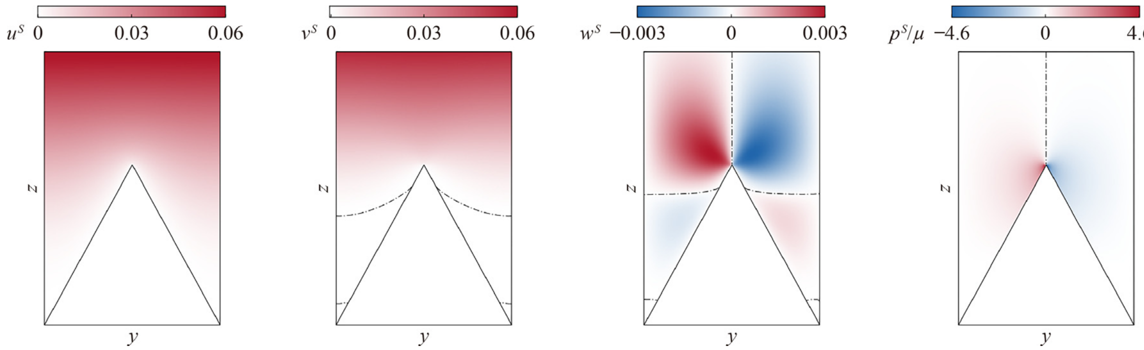

Fig. 2 Stokes solution around a periodic triangular riblet with a sharp 60° tip angle ($u^{\mathscr{S}}$ represents longitudinal component, $v^{\mathscr{S}}$ is transverse component and $w^{\mathscr{S}}$ is vertical one. $p^{\mathscr{S}}/\mu$ represents solution for pressure, presenting a singularity at tip, normalized by fluid dynamic viscosity).

the wall (the pressure at the wall is generally non-zero). We therefore interpolate the pressure across the riblet ensuring a smooth transition between the left and right sides.

Finally, a note on the spatial extent of the correction. Practically, we observe that the COCO coefficients $\lambda_j^{\mathscr{S}}$ decay to zero within roughly one grid spacing from the corner (assuming for simplicity $\Delta y = \Delta z$), and they smoothly blend into the IBM coefficients ($\lambda_j^{\mathscr{S}} = \lambda^{\mathscr{I}}$) when moving along the ribbed wall. For this reason, there is no need to calculate such coefficients far from the tip, as they will be zero and will not affect the solution. To avoid unnecessary calculations of the coefficients, we set the corner-correction radius to two times the larger grid spacing. Note that, since the hypothesis for the corner-correction application is that the viscous term is dominant, it should not be applied in regions outside the viscous sublayer. For this reason, one must make sure that the larger grid spacing in the riblet cross-section plane is smaller than the extent of the viscous sublayer (approximately 5 wall units). This condition is satisfied with margin in the present calculations.

3. Protrusion heights for triangular riblets with varying tip roundings

In this section we analyze the effect of tip rounding on triangular riblets. We consider three cross-sectional geometries with tip angles of 30°, 60° and 90°. For each geometry the tip rounding radius is varied and expressed as the nondimensional ratio r/s (rounding radius over riblet spacing). The investigated values span $r/s = 0$ (sharp tip) up to $r/s = 0.15$. A complete list of configurations, including the number of points per riblet spacing (n_{yr}), points per riblet height (n_{zr}), total points in the wall-normal direction (n_z), and the ratios s/δ or k/δ, is reported in Table 1. δ represents the channel semi height, k the riblet height. Note that for the sharp cases, a significantly higher grid resolution is needed in order to achieve grid-independent solutions. Stokes simulations follow the numerical setup outlined in Section 2 and employ the canonical immersed-boundary formulation of Luchini et al.[17] to represent the riblet geometry. The Stokes problem is essentially 2D, and the domain contains a single riblet with periodicity in the transverse (y) direction. In the wall-normal (z) direction the riblet-to-channel-height ratio is kept small (approximately 0.1). A unit centerline velocity is prescribed in both the longitudinal and transverse directions, which, with a unitary channel height, produces a unit velocity gradient in the far field and enforces a Couette-like forcing in both periodic directions. The riblet crest is located at $z = 0.5(l_{X,0} + l_{Y,0})$, where $l_{X,0}$ and $l_{Y,0}$ denote the longitudinal and transverse protrusion heights of the sharp configuration; such values are taken from Luchini et al.[4] for the available tip angles. Such configuration enables imposing a shear of approximately unity on both velocity components. Finally, to realize the Stokes limit ($Re \to 0$) the nonlinear terms in the Navier–Stokes equations are set to zero.

In Fig. 3 we present the protrusion heights values for the three considered geometries as a function of the tip rounding radius. The values are calculated for two different grids to prove the grid-independence of the results, with the fine grid presenting double the number of point per riblet (n_{yr}, n_{zr}) compared to the base grid. The parameters displayed in Table 1 refer to the base grid. Note that the three protrusion height values are adimensionalized with the square root of the groove cross section l_g, which decreases as the tip rounding radius is increased. The reference values from Luchini et al.[4] are available only for the $\alpha = 60°, 90°$ cases, and only for the sharp geometry ($r/s = 0$).

For all geometries the longitudinal protrusion height is the most affected by tip rounding, while the transverse one is weakly modified. Accordingly, Δh follows the behaviour of h_X, decreasing as the rounding radius increases, as expected since the riblets viscous performance (measured by Δh) is degraded by tip rounding. With respect to h_Y, tip rounding allows for a deeper penetration of the transverse flow into the riblet groove, effectively lowering the transverse flow virtual origin; yet it also reduces the crest vertical position. These competing effects therefore leave the protrusion height (the distance between crest and virtual origin) only weakly altered.

Interestingly, a smaller tip angle does not necessarily yield a larger Δh: for the sharp cases ($r/s = 0$) the largest Δh is obtained for $\alpha = 60°$, followed by $\alpha = 90°$ and then $\alpha = 30°$. Fig. 4 summarises the performance degradation for all geometries. We quantify degradation by the ratio $\Delta h/\Delta h_0$, where Δh_0 is the protrusion–height difference of the sharp geometry; this nondimensional measure facilitates comparison across cross sections. As expected, the impact of rounding grows as the tip angle decreases: at $r/s = 0.10$ the performance loss (relative

Table 1 Summary of geometric and discretization parameters for Stokes simulations.

Geometric	α	r/s	n_{yr}	n_{zr}	n_z	s/δ	k/δ
	30.0	0.000	124.0	129.0	567.0	0.055	0.094
	30.0	0.025	36.0	85.0	471.0	0.058	0.098
	30.0	0.050	36.0	84.0	471.0	0.060	0.102
	30.0	0.075	20.0	52.0	349.0	0.062	0.106
	30.0	0.100	20.0	51.0	347.0	0.065	0.111
	30.0	0.125	20.0	51.0	347.0	0.068	0.115
	30.0	0.150	20.0	50.0	345.0	0.070	0.120
	60.0	0.000	92.0	70.0	447.0	0.080	0.065
	60.0	0.025	32.0	48.0	397.0	0.083	0.067
	60.0	0.050	36.0	48.0	397.0	0.085	0.069
	60.0	0.075	24.0	39.0	371.0	0.087	0.072
	60.0	0.100	24.0	39.0	371.0	0.090	0.074
	60.0	0.125	24.0	39.0	371.0	0.092	0.076
	60.0	0.150	24.0	38.0	369.0	0.095	0.078
	90.0	0.000	60.0	41.0	387.0	0.105	0.050
	90.0	0.025	32.0	32.0	361.0	0.107	0.052
	90.0	0.050	32.0	32.0	361.0	0.110	0.053
	90.0	0.075	20.0	24.0	291.0	0.113	0.054
	90.0	0.100	20.0	24.0	291.0	0.115	0.055
	90.0	0.125	20.0	24.0	291.0	0.117	0.056
	90.0	0.150	20.0	23.0	291.0	0.120	0.058

Notes: α represents the riblet tip angle, r/s represents the ratio tip rounding radius to riblet spacing, n_{yr} and n_{zr} represent the number of points per riblet spacing and height, respectively. n_z represents the total number of points in the vertical direction in the domain, while s/δ and k/δ are the ratios spacing to channel height and riblet height to channel height.

to the sharp case) is about 28% for $\alpha = 30^\circ, 23\%$ for $\alpha = 60^\circ$ and 16% for $\alpha = 90^\circ$. This reduction in Δh corresponds to an equivalent decrease in the slope of the viscous regime roughness function ΔU^+.

When plotted against r/l_g, the ratio $\Delta h/\Delta h_0$ exhibits a clear exponential trend. Note that r/l_g is geometrically bounded for the triangular families considered, and the asymptotic value of Δh at the largest admissible r/l_g depends on α. We denote by Δh_∞ the value of Δh at the largest admissible r/l_g. In the limit $\alpha \to 0$ the largest-r/l_g shape becomes a semicircle, whereas for $\alpha \to \pi$ the shape tends to an almost flat surface; accordingly $\Delta h_\infty \approx 0$ for $\alpha \to \pi$, while Δh_∞ remains finite (that of a semicircular cross section) for $\alpha \to 0$. For the finite α values of the considered values, Δh_∞ reaches intermediate values between these two extremes.

The dashed curves on the right-hand side of Fig. 4 are analytical exponential fits of the form:

$$\frac{\Delta h}{\Delta h_0}(r/l_g) = \frac{\Delta h_\infty}{\Delta h_0} + \left(1 - \frac{\Delta h_\infty}{\Delta h_0}\right) \exp\left(\frac{r/l_g}{R}\right) \tag{8}$$

The fit parameters are the ratio $\frac{\Delta h_\infty}{\Delta h_0}$ and the characteristic decay length R; both vary with the tip angle α, and analytical expressions for these α dependencies are not readily available. For the $30^\circ, 60^\circ, 90^\circ$ geometries, the values for $\Delta h_\infty/\Delta h_0$ are, respectively, $(0.610, 0.606, 0.627)$, and for R $(0.0882, 0.187, 0.397)$.

4. Turbulent simulations

Inexpensive Stokes simulations provide Δh, which sets the slope of the viscous regime for riblets roughness function. However, when the riblet viscous size exceeds a certain threshold the viscous prediction no longer suffices to determine ΔU^+, and turbulent DNS are required. In this section, we present the results of turbulent simulations of channel flows over ribbed walls. We consider only the triangular cross-section shape with 60° tip angle at two different riblet viscous sizes. For each case, we vary the tip rounding radius to span the same r/s range as in Section 3. To cope with the high computational cost required for resolving the flow around such geometries, we employ the combined IBM/COCO approach outlined in Section 2, using a limited number of points to represent the riblets. The friction Reynolds number for all simulations is set to $Re_\tau = 200$, and statistics are averaged over approximately 85 large eddy turnover time units. The friction Reynolds number is adjusted using the actual friction velocity u_τ, which is computed from the total shear stress at the vertical coordinate corresponding to the virtual origin of turbulence. In particular, the virtual origin of turbulence, denoted z_T^+, is the z-coordinate located at a distance of l_T^+ below riblet tip. We determine z_T^+ as the vertical shift required to align the Reynolds shear stress profile of the ribbed case with that of the reference smooth case. Once z_T^+ is known, the friction velocity is

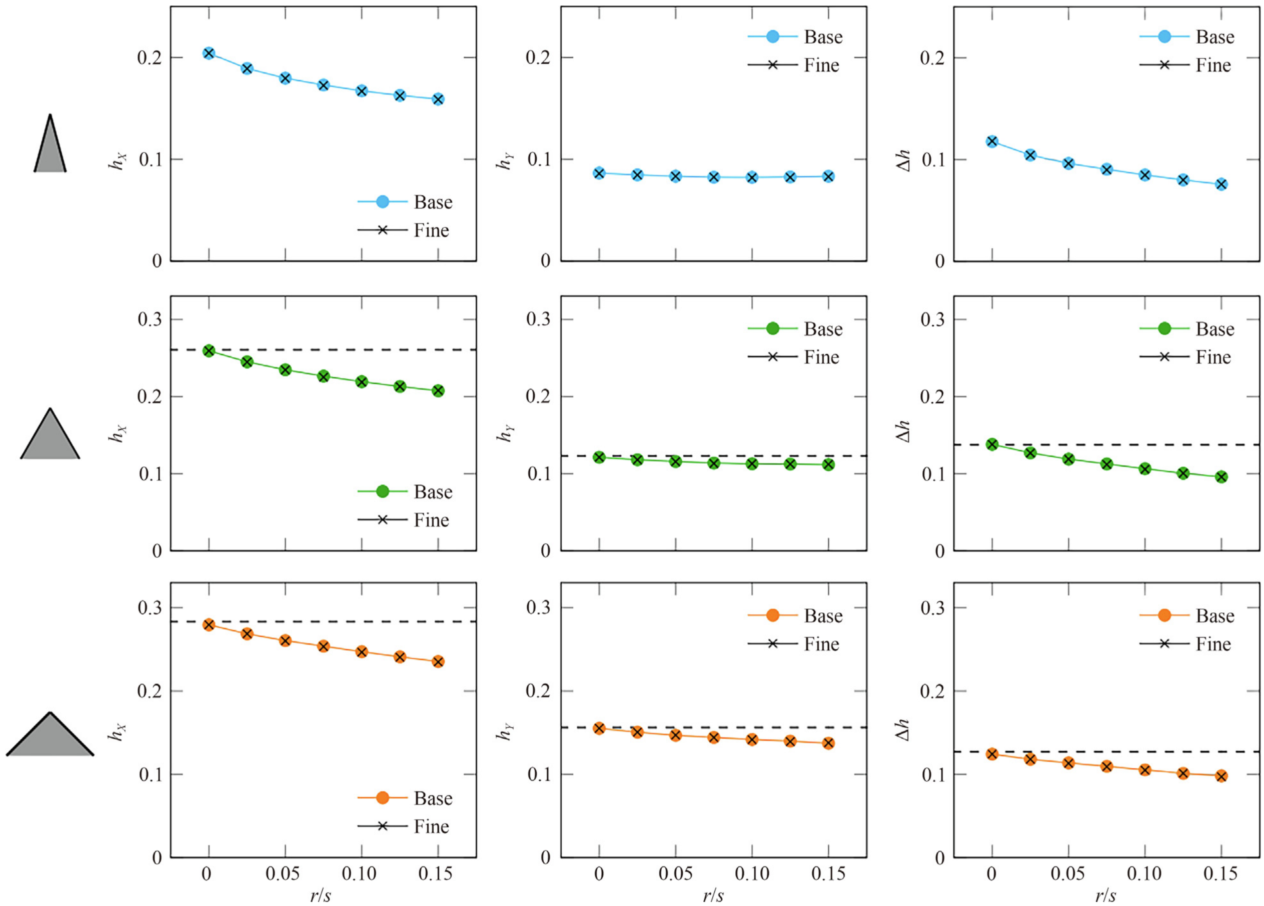

Fig. 3 Longitudinal (h_X), transverse (h_Y) protrusion heights and protrusion height difference (Δh) for three different cross section shapes, varying riblet tip rounding radius (r/s represents ratio rounding radius to spacing. Dashed lines correspond to sharp-tip limit values from Luchini et al.[4]).

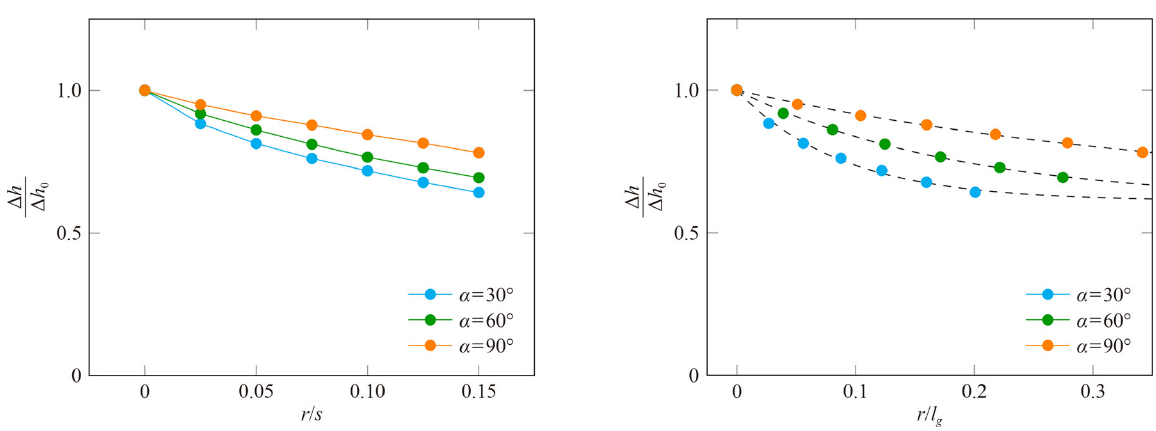

Fig. 4 Ratio between protrusion height difference of each case and protrusion height difference of sharp case (on left tip rounding radius is made dimensionless with riblet spacing, while on right square root of groove cross section is used for adimensionalization. Dashed lines represent an exponential fit for three different cross sections).

calculated as $u_\tau = u_{\tau,0}\sqrt{1 - z_T}$, where $u_{\tau,0}$ is the friction velocity of the reference smooth case. The procedure follows what is described in Ibrahim et al.[3] A summary of discretization and simulation parameters for all simulated cases is presented in Table 2.

The corner-correction enables a coarse discretization of the domain around the riblets, with 16 points per riblet spacing used in the spanwise direction. In the wall-normal direction, a geometric spacing distribution is employed, with Δz^+ equal to 0.8 at the wall and 2.4 at the channel centerline. This results

Table 2 Geometric and discretization parameters for turbulent simulations.

l_g^+	s^+	r/s	Re_τ	L_x	L_y	n_x	n_y	n_z	n_{yr}	n_{zr}
5.2	8	0.000	198.5	7.5	3.76	752	1504	345	16	8
5.1	8	0.025	198.6	7.5	3.76	752	1504	345	16	8
4.9	8	0.050	198.6	7.5	3.76	752	1504	345	16	8
4.8	8	0.075	198.8	7.5	3.76	752	1504	345	16	8
4.6	8	0.100	198.8	7.5	3.76	752	1504	345	16	8
4.5	8	0.125	198.9	7.5	3.76	752	1504	345	16	7
4.3	8	0.150	199.0	7.5	3.76	752	1504	345	16	7
10.4	16	0.000	197.3	7.5	3.76	752	752	353	16	17
10.1	16	0.025	197.4	7.5	3.76	752	752	353	16	17
9.8	16	0.050	197.5	7.5	3.76	752	752	353	16	16
9.5	16	0.075	197.6	7.5	3.76	752	752	353	16	16
9.2	16	0.100	197.9	7.5	3.76	752	752	353	16	15
8.9	16	0.125	198.0	7.5	3.76	752	752	353	16	15
8.7	16	0.150	198.1	7.5	3.76	752	752	353	16	14

Notes: l_g^+ represents the square root of the groove cross section, s^+ the riblet spacing, r/s the ratio rounding radius to riblet spacing, Re_τ the friction Reynolds number, L_x and L_y the domain dimensions in the periodic directions, n_x, n_y and n_z the number of points in the stream-, spanwise and wall-normal directions, respectively, while n_{yr}, n_{zr} indicate the number of points per riblet spacing and height.

in approximately 8 grid points per riblet height ($n_{zr} \approx 8$) for the $s^+ = 8$ cases and approximately 16 grid points per riblet height ($n_{zr} \approx 16$) for the $s^+ = 16$ cases. While the resolution is considerably coarser than that used in the Stokes simulations, the corner-correction should allow for proper flow discretization around the riblet geometries even with this reduced number of points. All simulations were carried out on an identical grid with and without the corner-correction, to assess the impact of the proposed methodology on accuracy.

Since the physical riblet spacing is kept constant in all simulations, the rounding of the tip angle modifies the l_g value. To compare the ΔU^+ values of geometries with different r/s ratios, we must ensure that the l_g^+ values are consistent. For the $s^+ = 8$ cases, the discrepancy arising from different l_g^+ values can be accounted for by recognizing that in the viscous regime ($s^+ < 10$) the roughness function varies linearly with the riblet size. In these cases, it is possible to correct the ΔU^+ value as follows:

$$\Delta U_c^+ = \Delta U^+ - \Delta h \Delta l_g^+ \tag{9}$$

where ΔU_c^+ is the corrected ΔU^+ at the reference l_g^+ value of the sharp configuration, Δh is the difference in the two protrusion heights taken from the results in Section 3, and Δl_g^+ is the difference between the l_g^+ values of the sharp and rounded geometries.

For the $s^+ = 16$ cases, correcting the computed ΔU^+ values is less straightforward, as these riblet dimensions do not fall into the viscous regime and the roughness function is not linear with respect to l_g^+. However, since the drag reduction peak occurs around $l_g^+ = 11$, we can assume that for such l_g^+ values the dependence of ΔU^+ on the riblet size is weak (at the peak, the ΔU^+ gradient is zero). For this reason, the drag reduction values for the $s^+ \approx 16$ cases are not corrected.

Fig. 5 presents the ΔU^+ values for all simulated geometries as a function of the tip rounding radius r/l_g. As expected, all geometries with tip rounding achieve smaller drag reduction values compared to the sharp geometry. The dashed lines represent the viscous drag reduction contribution $\Delta U_v^+ = -\Delta h\, l_g^+$ for all geometries at the considered l_g^+ value. For the $s^+ = 8$ cases, the l_g^+ value used is that of the sharp geometry, consistent with Eq. (9), while for the $s^+ = 16$ cases, the exact l_g^+ value for each geometry is used from Table 2. Notably, for the $s^+ = 8$ cases, the ΔU_c^+ values align well with the viscous prediction. This is because these viscous sizes are small enough to fall within the viscous regime, where the Δh value alone is sufficient to characterize riblet performance in turbulent flow. In contrast, for the $s^+ = 16$ cases, the viscous prediction ΔU_v^+ presents significantly larger drag reduction values compared to the actual measurements. Indeed, when riblets have a viscous size of $l_g^+ \approx 10$, drag-increasing effects emerge, and the measured ΔU^+ values are smaller in magnitude compared to the value ΔU_v^+.

The curve from the viscous prediction follows the same behaviour as the roughness function, indicating that the primary effect of tip rounding is a decrease in the viscous Δh value. The oscillating behaviour of the ΔU^+ values from the $s^+ = 8$ cases is likely attributable to the finite simulation time and partially to the coarse grid resolution, which employs only approximately 8 points per riblet height in the wall-normal direction.

The results in Fig. 5 are compared to those obtained with the simple IBM from Luchini et al.,[17] to assess the impact of the corner-correction. While for the rounded cases the obtained ΔU^+ values are weakly affected by the use of the corner-correction, the sharp cases present significantly different results, showing how such sharp geometries would typically require a very high grid resolution in order to obtain grid-independent results.

This could be anticipated by looking at the number of points per riblet needed to obtain accurate protrusion height values for the Stokes cases, as Table 1 indicate that the sharp cases require a much higher number of points per riblet compared to the rounded cases.

For reference, a ΔU^+ value for the same sharp cross-section shape is also shown in Fig. 5, taken from Wong et al. [18] Such

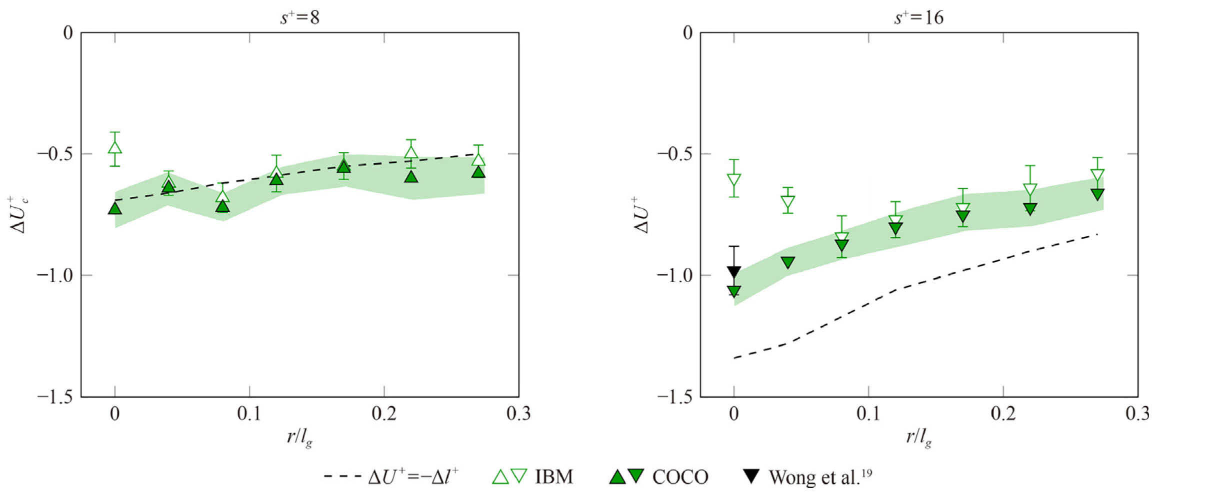

Fig. 5 ΔU^+ values computed for considered riblet geometries at two viscous spacings as a function of riblet tip rounding radius (non-dimensionalized with l_g value) (shaded area indicates temporal uncertainty of measurement with a 95% confidence interval for cases run with corner-correction (COCO). For other cases temporal uncertainty is shown as an error bar. Dashed lines indicate viscous prediction ΔU_v^+. Black marker represents ΔU^+ value for the same cross section shape at $l_g^+ = 9.7$ from Wong et al.[18]).

value reasonably aligned with the one obtained with the corner-correction, supporting the validity of the presented methodology. Note that the geometry from Wong et al.[18] presents a slightly smaller viscous size ($l_g^+ = 9.7$), and such simulation has been performed at a friction Reynolds number of $Re_\tau = 395$.

The shaded areas and the error bars in Fig. 5 indicate the uncertainty arising from the finite simulation time, with a 95% confidence interval, in which the standard deviation of the measure is computed with the adaptive-batch-size algorithm from Russo and Luchini.[19]

5. Conclusions

In this paper, we have presented results on Stokes and turbulent flows over riblets. Through Stokes simulations, we investigated the viscous behaviour of triangular riblets with different cross-sectional shapes across various tip rounding radius values. Our results demonstrate that in all cases, riblet performance, as measured by Δh, decays as the rounding radius increases, with the decrease following an exponential curve. The rate of Δh reduction is more pronounced for riblets with larger height-to-spacing ratios.

Turbulent simulations were performed to assess riblet behaviour at two different viscous sizes. For the smaller riblet sizes, which fall within the viscous regime, we observed close agreement with the viscous prediction. For the larger riblet sizes, an offset between the viscous prediction and the actual measurements emerges due to the loss of linearity in the roughness function. Nevertheless, the same performance degradation with tip rounding is observed across all cases, confirming that tip geometry plays a critical role in riblet effectiveness regardless of the operating regime.

CRediT authorship contribution statement

Stefano CIPELLI: Writing – original draft, Visualization, Validation, Software, Methodology, Investigation, Formal analysis, Data curation, Conceptualization.**Giacomo RONCHETTI**: Software, Methodology, Investigation, Formal analysis. **Davide GATTI**: Writing – review & editing, Supervision, Software, Resources, Project administration, Methodology, Investigation, Conceptualization.

Declaration of competing interest

The authors declare that they have no known competing financial interests or personal relationships that could have appeared to influence the work reported in this paper.

Acknowledgments

The authors acknowledge M. Quadrio and P. Luchini for insightful discussions and for guidance on the formulation and implementation of the immersed-boundary method used in the simulations. This work was supported by the Deutsche Forschungsgemeinschaft (DFG), Germany (No. 423710075).

References

1. Walsh MJ. Drag Characteristics of V-Groove and Transverse Curvature Riblets. In Hough Gr, editor. *Viscous flow drag reduction*. Reston: AIAA; 1980. p.168-84.
2. Bechert D, Reif W. On the Drag Reduction of the Shark Skin. *23rd aerospace sciences meetings*. Reston: AIAA; 1985.
3. Ibrahim JI, Gomez-de-Segura G, Chung D, et al. The smooth-wall-like behaviour of turbulence over drag-altering surfaces: A unifying virtual-origin framework. *J Fluid Mech* 2021;**915**:A56.
4. Luchini P, Manzo F, Pozzi A. Resistance of a grooved surface to parallel flow and cross-flow. *J Fluid Mech* 1991;**228**:87–109.
5. Bechert DW, Bruse M, Hage W, et al. Experiments on drag-reducing surfaces and their optimization with an adjustable geometry. *J Fluid Mech* 1997;**338**:59–87.
6. Choi H, Moin P, Kim J. Direct numerical simulation of turbulent flow over riblets. *J Fluid Mech* 1993;**255**:503–39, Oct.
7. Modesti D, Endrikat S, Hutchins N, et al. Dispersive stresses in turbulent flow over riblets. *J Fluid Mech* 2021;**917**:A55.

8. Garcia-Mayoral R, Jiménez J. Hydrodynamic stability and the breakdown of the viscous regime over riblets. *J Fluid Mech* 2011;**678**:317–47.
9. Endrikat S, Modesti D, García-Mayoral R, et al. Influence of riblet shapes on the occurrence of kelvin-helmholtz rollers. *J Fluid Mech* 2021;**913**:A37.
10. Jiménez J. Turbulent flows over rough walls. *Annu Rev Fluid Mech* 2004;**36**(1):173–96.
11. von Deyn LH, Gatti D, Frohnapfel B. From drag-reducing riblets to drag-increasing ridges. *J Fluid Mech* 2022;**951**:A16.
12. García-Mayoral R, Jiménez J. Drag Reduction by riblets. *Philos Trans Roy Soc A* 2011;**369**(1940):1412–27.
13. Luchini P. Immersed-boundary simulations of turbulent flow past a sinusoidally undulated river bottom. *Eur J Mech B* 2016;**55**:340–7.
14. Mohan Rai M, Moin P. Direct simulations of turbulent flow using finite-difference schemes. *J Comput Phys* 1991;**96**:15–53.
15. Orlandi P. *Fluid flow phenomena: A numerical toolkit*. Dordrecht: Kluwer Academic Publishers; 2006. p. 8–39.
16. Moffatt HK. Singularities in fluid mechanics. *Phys Rev Fluids* 2019;**4**(11):110502.
17. Luchini P, Gatti D, Chiarini A, et al. A simple and efficient second-order immersed-boundary method for the incompressible Navier-Stokes equations. *J Comput Phys* 2025;**539**:114245.
18. Wong J, Camobreco CJ, García-Mayoral R, et al. A viscous vortex model for predicting the drag reduction of riblet surfaces. *J Fluid Mech* 2024;**978**:A18.
19. Russo S, Luchini P. A fast algorithm for the estimation of statistical error in DNS (or experimental) time averages. *J Comput Phys* 2017;**347**:328–40.